ADVANCED MATERIALS TECHNOLOGIES
www.advmattechnol.de

Wearable, Wireless, Stretchable, High-Density Surface Electromyography Interface

*Yi Zhao, Ningbin Zhang, Jinhao Li, Jieji Ren, and Guoying Gu**

Surface electromyography (sEMG) provides rich neural information as the human-machine interfaces. However, it is still challenging to achieve wearable sEMG-based human-machine interfaces, owing to the non-conformal electrode arrays and bulky monitoring systems. Herein, a wearable, wireless, and high-density sEMG interface incorporating soft multi-channel electrode arrays and a minimized signal monitoring circuit is presented. The stretchable (≈150%) electrode array fabricated by 3D printing silver paste onto adhesive (0.37 N cm^{-1}) silicone-based substrates demonstrates the capability of eliminating signal artifacts in dynamic hand motions. The electrode array with a customize wireless circuit is further integrated for real-time recording of eight-channel sEMG signals on deforming skin. Using this conformal system, various wrist-hand gesture recognition is achieved through single flexor digitorum superficialis (FDS) muscle detection. The wireless sEMG-based interface also enables high-precision signal monitoring under dynamic exercises of the upper and lower limbs, exploring the diverse applications for human-machine interaction and daily healthcare.

1. Introduction

Surface electromyography (sEMG) is the electrical biosignal that accompanies muscle contraction, containing rich α motor nerve information.[1] As a vital technology at the human-machine interface, sEMG electrodes enable non-invasive obtaining of human motion intentions and muscle status for prosthetic control and healthcare.[2–6] Notably, the high-precision monitoring of sEMG signals, especially for deforming muscles, plays a vital role in gesture recognition and fatigue detection.[7,8] However, the repeated movement of muscles introduces significant motion artifacts at the unstable skin-electrode interface.[9] The physical restraints of the bulky collection device also challenge the effective integration of conformal systems for exercise. Thus, it remains elusive to construct a wearable, high-density sEMG interface for on-body monitoring.

Adopting soft materials to construct conformal devices is one promising route to establish the stable sEMG interface.[10,11] For example, recent efforts have been devoted to synthesizing stretchable conductive materials and designing deformation-tolerant structures for electrode arrays.[12–22] Various stretchable electrode arrays are further manufactured to enable sEMG recording on curved skin surfaces based on complicated fabrication processes.[23–28] Meanwhile, the adhesion of electrodes to the skin often requires additional tapes, which restricts the conformal deformation. To address this issue, diverse adhesive groups (e.g., tannic acid and hydrogel matrix polyacrylamide) have been introduced into conductive polymer networks to decrease the interference in signal acquisition.[29–34] However, the bridging interface between soft materials and rigid processing circuits limits the stable multi-channel monitoring in exercise.[35–40] Hence, existing techniques are still struggling to achieve stretchable, miniaturized sEMG-based human-machine interfaces.

In this article, we report a wearable, wireless, and high-density sEMG interface consisting of 3D-printed multi-channel electrode arrays and a minimized wireless signal monitoring circuit (**Figure 1**). We first construct a three-layer sandwiched soft electrode array by all 3D printing methods. The electrode array, containing stretchable silver paths (≈150%) and adhesive silicone-based substrates (0.37 N cm^{-1}), enables a reliable and conformal skin-electrode interface to eliminate motion artifacts. By applying to the thumb joint, our electrode records high signal-to-ratio (SNR) sEMG signals (>23 dB) under dynamic tasks without losing subtle information. We further design a minimized, wireless multi-channel system to monitor real-time high-density sEMG signals, accompanied by data transmission through the Bluetooth module. This integrated system demonstrates the capability for various wrist-hand gesture recognition with an average accuracy of 92.6% through single FDS muscle detection. Our sEMG-based human-machine interface enables high-precision on-body monitoring under dynamic exercise of upper and lower limbs, such as dumbbell training and stepping.

Y. Zhao, N. Zhang, J. Li, J. Ren, G. Gu
Robotics Institute and State Key Laboratory of Mechanical System and Vibration
School of Mechanical Engineering
Shanghai Jiao Tong University
Shanghai 200240, China
E-mail: guguoying@sjtu.edu.cn
Y. Zhao, J. Li, G. Gu
Shanghai Key Laboratory of Intelligent Robotics
Meta Robotics Institute
Shanghai Jiao Tong University
Shanghai 200240, China

The ORCID identification number(s) for the author(s) of this article can be found under https://doi.org/10.1002/admt.202500607

DOI: 10.1002/admt.202500607

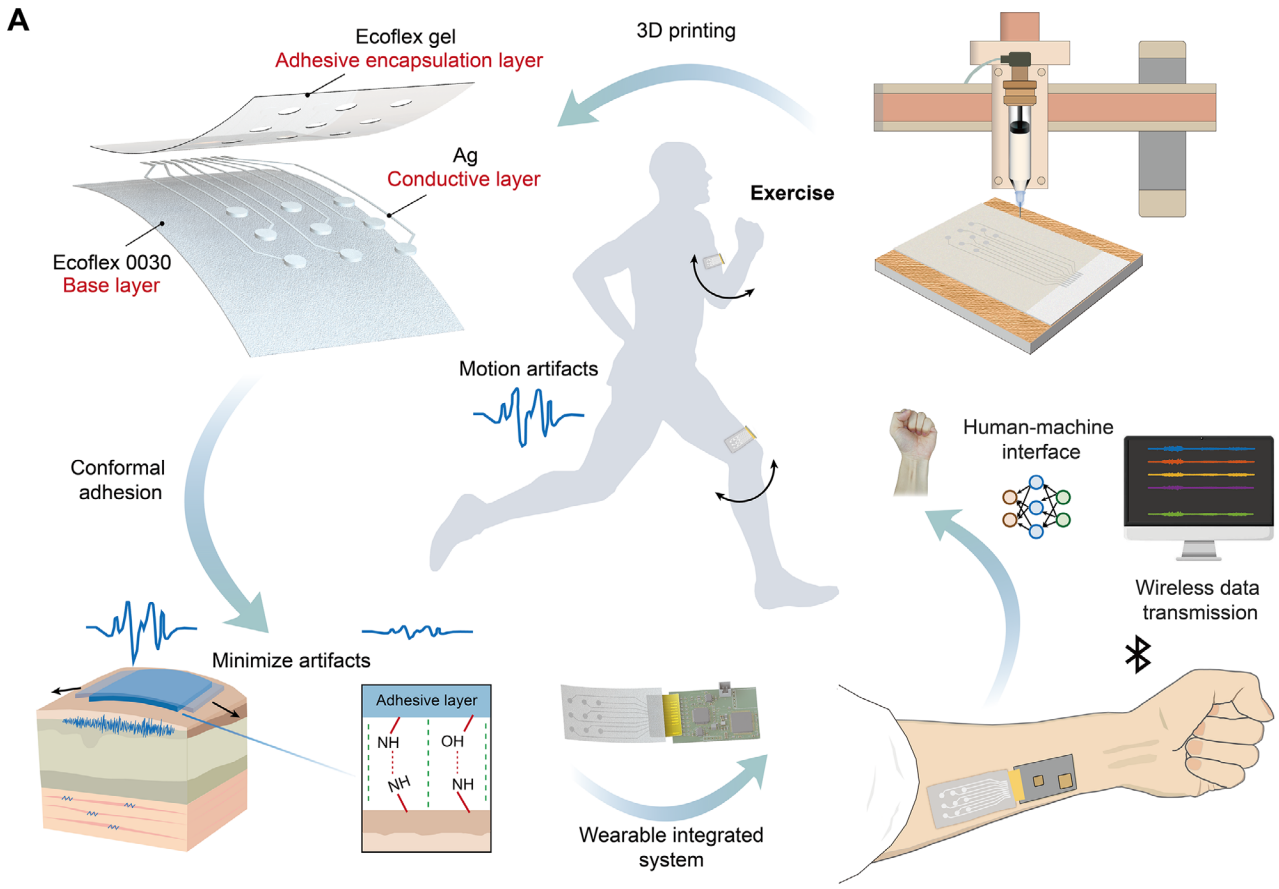

Figure 1. Overview of the wearable, wireless, and stretchable high-density sEMG interface. A) Schematic diagram of the wearable, wireless, and stretchable sEMG interface for low motion artifact monitoring and hand gesture recognition. The highly stretchable adhesive electrode is manufactured by integrated 3D printing. Due to the high stretchability of the electrode and the adhesion of the encapsulation layer, it can establish good conformal ability with the skin to reduce motion artifacts. System integration of the stretchable high-density electrode can enable the wearable sEMG interface to achieve real-time monitoring of low-motion artifacts during exercise and realize human-machine interface applications such as hand gesture recognition. B) The printed high-density electrode can withstand large stretching, twisting, and rubbing deformation, and recover to its initial shape once the stress is removed. C) Printed electrodes adhere conformally to the skin surface of the thumb joint.

2. Results

2.1. Design of the Stretchable High-Density Electrode

We design the stretchable high-density electrode array as a sandwich-like film with a size of 60 × 40 mm, including the base layer, the conductive layer, and the adhesive encapsulation layer from bottom to top (Figure 1A). We choose Ecoflex 0030 silicone rubber as the base layer for the low Young's modulus (69 kPa) and high stretchability (≈150%). To detect spatial sEMG signals in uniform distribution, we arrange 9-channel silver conductive paths into a 3 × 3 symmetric array, where the diameter and

spacing of circular electrodes are 4 and 8 mm, respectively. Given the compatibility between materials and following used DIW process, the viscoelasticity of the material needs to be printable to avoid problems such as nozzle clogged caused by excessively high viscoelasticity or inability to shape due to insufficient viscoelasticity. It is also necessary to avoid issues such as material leakage and water loss, which may affect the practical application of the system. Herein, we adopt a stretchable silver paste to form robust conductive paths, where micro silver flakes overlap to form deformable conductive paths (Figure 1B,C; Figure S1, Supporting Information). We also introduce a multi-hole Ecoflex gel encapsulation layer to avoid signal crosstalk and provide stable adhesion to skins by hydrogen bonds and Van Der Waals forces, which can expose convex circular electrodes for robust skin-electrode conductive paths. We further optimize the mixing ratio of Ecoflex gel agents for stronger interfacial adhesion. The standard 90° peeling test shows that the peeling force for the encapsulation layer increases as the proportion of the cross-linking agent decreases (Figure S2, Supporting Information) while extending the curing time of Ecoflex gel. Due to the decrease in the proportion of crosslinking agents, local incomplete curing may occur on the surface of the Ecoflex gel, resulting in an increase in surface viscosity. To balance the enhanced adhesion performance and extended curing time, we choose the cross-linking agent of 25 wt.% for the adhesive silicone to obtain a peeling force of 0.37 N cm^{-1} without synthesizing any new materials and intricate structures (Figure S3, Supporting Information). To showcase the adhesion capability for different materials, the optimized Ecoflex gel can stably adhere to objects of similar weight but different shapes, including tangerines, wooden blocks, and tape, by being fixed in the palm of the hand. Moreover, we further investigate the effect of thickness on the adhesion force based on the optimized Ecoflex gel. Two types of thin films with 1 and 3 mm thickness are used for the standard 90° peeling test (Figure S4, Supporting Information). The results show that a thicker adhesive layer can generate a stronger adhesion force. Combining the above features, our soft electrode array exhibits compliant and mechanical robustness to withstand deformations such as stretching, twisting, and rubbing (Figure 1B; Figure S5 and Movie S1, Supporting Information).

2.2. Fabrication of the Stretchable High-Density Electrode

Next, we present an all-printed fabrication process to simplify the procedure and achieve continuous customized manufacturing of each functional layer (**Figure 2**). It is worth noting that each printing layer has unique structures, including the rectangular plane, polylines, the hollow plane, and the convex cylinder. To achieve accurate printing of the whole predesigned structure, we perform multi-material printing characterization of printing linewidth and plane height for each functional layer based on the DIW mechanism.

Figure 2A illustrates the detailed mechanism of the DIW process and critical printing parameters of filaments,[41] including printing speed, printing height, extrusion pressure, and nozzle diameter. In addition, infill line distance, the spacing between adjacent filaments, can further influence the plane height of printing layers. To reduce the variables and investigate the impact of the main factors,[42] we first investigate the printing linewidth under varying pressure and printing speed, while the parameters of the printing height and nozzle diameter are preset. Furthermore, based on the characterization results, we choose rational printing parameters and study the relationship between infill line distance and plane height. Considering the capillary effect between extrusion inks and substrates, printing substrates vary according to the stacking relationship of electrode materials. For the conductive Ag ink, the printing experiment is conducted on an Ecoflex 0030 substrate with a printing height of 0.1 mm and a printing nozzle diameter of 0.24 mm (Figure 2B). For the adhesive Ecoflex gel ink, the printing height is set as 0.3 mm and the printing nozzle diameter is set as 0.34 mm with the same substrate of Ecoflex 0030. Meanwhile, the printing height is set as 0.3 mm and the printing nozzle diameter is set as 0.26 mm with ease release agent-covered PI substrate for Ecoflex 0030 ink (Figure 2C). The results show that the printing linewidth continuously changes as an inverse proportional function. Then we select a printing parameter of 200 kPa and 2 mm s^{-1} for the Ag ink to improve the stretchability by obtaining relatively wide conductive lines. To ensure fast manufacturing while maintaining sufficient printing accuracy, the printing parameter of the Ecoflex 0030 is selected as 200 kPa and 5 mm s^{-1}. To further achieve a relatively thick adhesive layer with stronger adhesion, the printing parameter of the Ecoflex gel is selected as 300 kPa and 3 mm s^{-1}. We further study the panel height and infill line distance based on the chosen extrusion pressure and printing speed (Figure 2D,E), which shows that the height of the printing plane decreases with increasing infill line distance. Hence, we hope to increase the thickness of the adhesive layer while maintaining the overall thinness of the electrode, in order to enhance the conformal ability of electrode arrays.[10] Based on the quantitative printing parameters, we finally formulate printing patterns with reasonable infill line distance for each function layer (0.6 mm for the base layer of 150 μm height, 0.1 mm for the conductive circular electrode of 290 μm height, and 0.8 mm for adhesive encapsulation layer of 275 μm), ultimately determining an overall electrode thickness of 440 μm (Figure S6, Supporting Information). Subsequently, the electrode array is printed layer by layer to achieve continuous fabrication (Figure 2F and Movie S2, Supporting Information). To facilitate the detachment of silicone rubber, we spray the ease release agent on the PI sacrificial layer ahead of printing. Moreover, we treat the surface of the electrode array with plasma and peel it off from the PI sacrificial layer, before sticking it to the flexible transfer circuit by anisotropic conductive film (ACF) tapes. By squeezing the electrode array with metal pens, the printed electrode exhibits a robust material interface to resist deformation, demonstrating reliable structural stability (Figure S7 and Movie S3, Supporting Information).

2.3. Characterization of the Printed Stretchable Electrode

We characterize the electrical and mechanical properties of the printed electrode array (**Figure 3**). We first conduct the electrochemical impedance spectroscopy (EIS) of electrodes with varying diameters based on the standard three-electrode method.[43] The overall impedance of electrodes gradually decreases with the increasing scanning frequency, and the small-diameter electrodes have a lower skin-electrode impedance at low-frequency

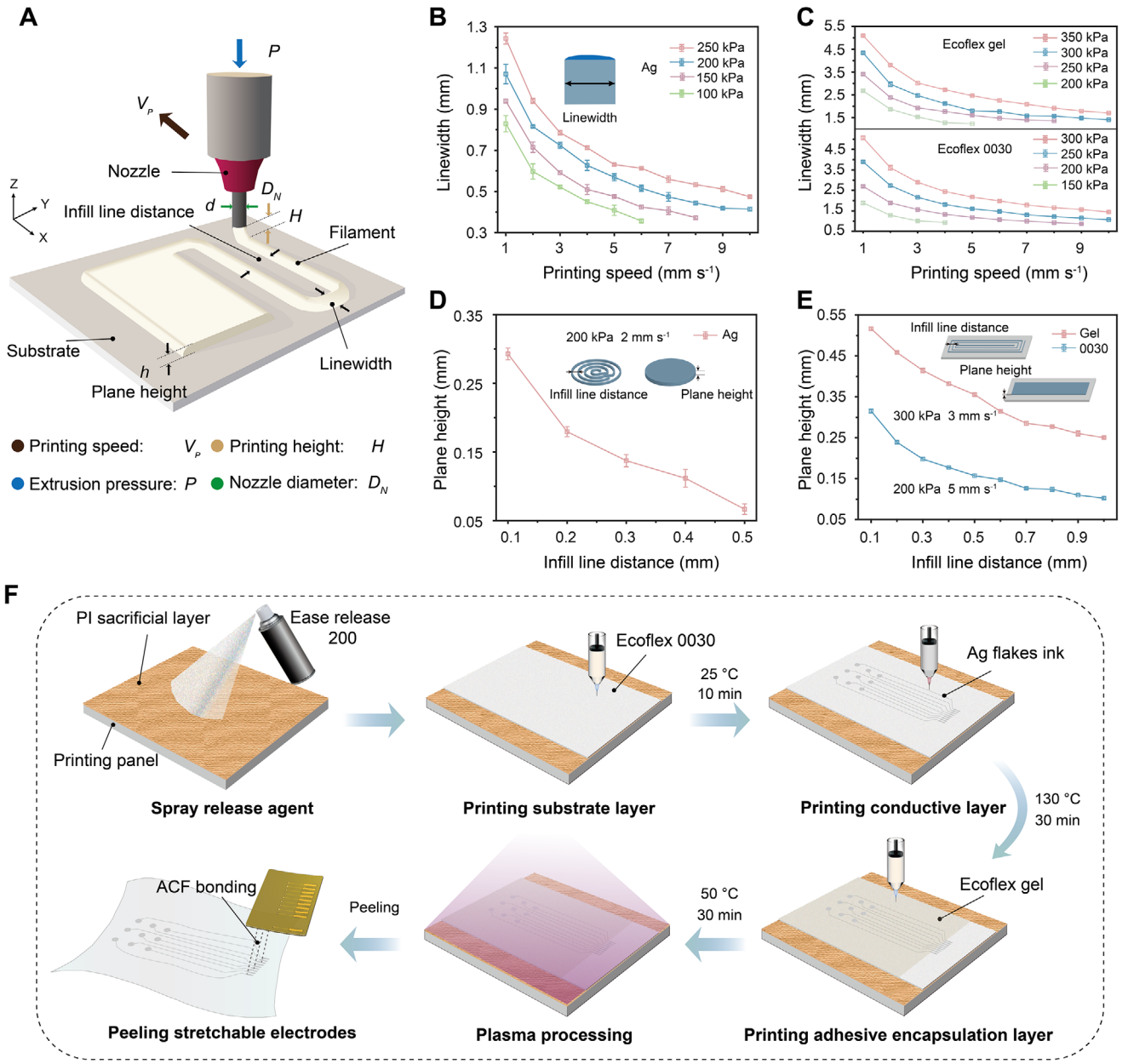

Figure 2. Fabrication of the high-density electrode via 3D printing. A) Schematic illustration of the high-precision DIW printing. B) The relationship between the linewidth of Ag filaments and the printing speed under varying pressures on the Ecoflex 0030 substrate. The printing height is set as 0.1 mm with the 0.24 mm nozzle. C) The relationship between the linewidth of silicone rubber filaments and the printing speed under varying pressures. The Ecoflex gel ink is printed on the Ecoflex 0030 substrate with 0.3 mm printing height and 0.34 mm nozzle. The Ecoflex 0030 ink is printed on the PI substrate with 0.3 mm printing height and 0.26 mm nozzle. D) The relationship between the printing plane height and the infill line distance under chosen printing parameters for Ag ink. E) The relationship between the printing plane height and the infill line distance under chosen printing parameters for Ecoflex gel and Ecoflex 0030. F) 3D printing fabrication process of the high-density electrode array for all functional layers. The base layer, conductive layer, and adhesive encapsulation layer are printed continuously, with heating and curing treatment interspersed in between. The sacrificial layer facilitates the peeling and use of electrodes, while plasma treatment is used to enhance the adhesion of ACF tape.

fields (Figure 3A; Figure S8, Supporting Information). This may be attributed to that the small-diameter electrodes have a larger adhesive area, which enables a tight conductive connection with the skin. In contrast, large electrode sizes sacrifice the stable contact and result in relatively large skin-electrode impedance (Figure S9, Supporting Information). Meanwhile, standard 90° peeling tests examine the adhesion performance for the skin-electrode interface, displaying continuous, and stable adhesiveness with maximum debonding resistance point (Figure 3B). In addition, we perform the cyclic stretching test to simulate the deformation of the skin (typically strain $\varepsilon < 20\%$) in actual use. The results show that the printed electrode can maintain a

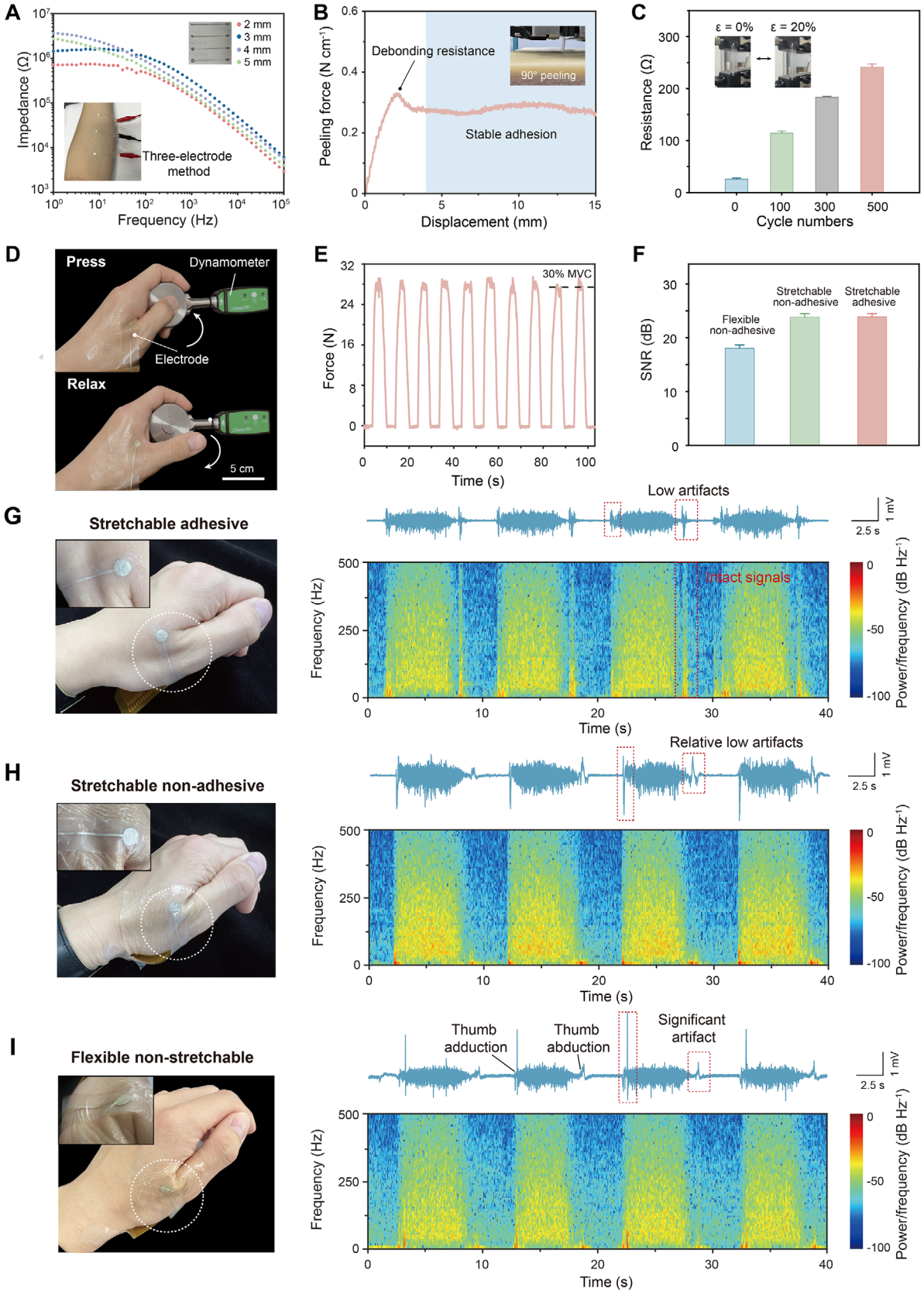

resistance of several hundred ohms even when stretched over 500 times, which still satisfies the requirement of sEMG recording (Figure 3C). Note that the silver paste wrapped in silicone may cause cracks in the silver flakes after being stretched cyclically, resulting in a resistance increase of the printed electrodes. We further evaluate the recording performance of sEMG signals under dynamic motion tasks by using our stretchable adhesive electrode. We print three types of electrodes (stretchable adhesive electrodes, stretchable non-adhesive electrodes, and flexible non-stretchable electrodes) to demonstrate the effect of stretchability and adhesiveness on minimizing the motion artifact (see Figure S10 for detailed electrode structures, Supporting Information). By adhering these electrodes above the dorsal interosseous muscle of the thumb (Figure 3D), the recruited subjects are required to press the dynamometer cyclically under 30% maximum voluntary force (MVC) and continuously switch between press and rest state (Figure 3E). As shown in Figure 3F, the collected sEMG signals exhibit that electrode stretchability enables a higher SNR. The results show that stretchable electrodes have similar SNR ratios and are both higher than the non-stretchable ones regardless of adhesion. Meanwhile, the adhesive one can adhere to the skin of subjects without any external adhesive tape, which can greatly enhance the user experience and reduce constraints on the moving joints. We further transform the time-domain signals into the time-frequency space (Figure 3G–I). The results show our stretchable adhesive electrode array can minimize the motion artifacts at the initial stage of thumb adduction and thumb abduction (Figure S11, Supporting Information). Benefiting from the stable skin-electrode interface, our electrode also enables the monitoring of subtle sEMG signals. For example, when the thumb leaves the surface of the force dynamometer, our electrode array has less signal loss in monitoring the movement of the thumb lifting.

2.4. Wearable Integrated sEMG Human-Machine Interface

Next, we integrate the electrode array with a wireless monitoring circuit to recognize various wrist-hand gestures as the human-machine interface (**Figure 4** and Table S1, Supporting Information). The presented integration strategy consists of the hardware electrode module and the user interface visualization module. The hardware electrode module is responsible for achieving the recording of analog sEMG signals by integrating printed stretchable electrode arrays, flexible transfer circuits, miniaturized signal recording circuits, the Bluetooth module, and the battery (Figure 4A; Figures S12–S15, Supporting Information). We utilize a biological signal acquisition chip ADS1299 to achieve 8-channel sEMG signal monitoring through the method of multiplexing for 1000 Hz frequency. The collected signals are transmitted to the MCU chip through serial peripheral interface (SPI) communication protocol and then divided into data packets for wireless transmission through a Bluetooth module. Although the minimized system adopts PCB circuits to ensure the stability of signal transmission, the overall size is only 60 × 36 mm, which will not significantly affect the overall wearability. Note that all the power consumption of the hardware device is converted into the required voltage for each module through a 3.3 V lithium battery. Finally, all data packets are obtained and unpacked on the customized user interface for real-time sEMG visualization and data storage (Figure 4B; Figure S16, Supporting Information).

We further use this integrated system to recognize and classify various wrist-hand gestures (Figure 4C–F; Figure S17, Supporting Information). We adhere the wearable sEMG human-machine interface to the skin above the FDS muscle of the upper arm (Figure 4C). Then, the subject performs seven consecutive gestures including rest, index pinch, middle pinch, ring pinch, fist, wrist flexion, and thumb flexion, where each gesture holds for 10 s and rests for another 10 s among them. The representative 8-channel sEMG signals recorded by using our human-machine interface are shown in Figure 4D. We further use a 150 ms sliding window to extract time domain (TD) features into the support vector machine (SVM) machine learning algorithm. After offline classification training, we can recognize seven types of wrist-hand gestures mentioned above (Figure 4E; Figure S18, Supporting Information). The confusion matrix of classification results shows that almost all gestures achieve an offline classification accuracy of over 90% (Figure 4F), except for fist and wrist flexion. The squeezing force of the ring finger can cause other fingers to bend synergistically and mislead a part of the fist to be identified as the ring finger pinching. Overall, the gesture recognition experiment based on a single muscle group achieves a high classification accuracy of 92.6% for seven fine hand gestures including wrist and finger movements, due to the comprehensive temporal and spatial information provided by the wearable, high-density sEMG human-machine interface (Figure S19, Supporting Information).

2.5. Application of Wearable Integrated sEMG Interface for Dynamic Exercise

To further demonstrate the high-precision monitoring capability under dynamic deformation, we apply our wearable integrated sEMG interface and a commercial electrode system (as the control group) to record the signals of adjacent muscle regions simultaneously. We select the vastus medialis muscle and the biceps brachii muscle as the monitoring target, which undertakes the stretching movements of lower and upper limb joints in exercise (**Figure 5**A,B). The subjects are required to perform the exercises continuously and randomly, including squatting, stepping, dumbbell curl, and dumbbell front raise (Movie S4,

Figure 3. Characterization of the printed stretchable electrode. A) Comparison of bode diagram of the impedance moduli between different sizes of the printed stretchable electrode. B) Peeling force of the adhesive electrode. C) Durability test of cyclic stretching. D) Image of the experimental setup of dynamic pressing with the three types of printed electrodes pasted on the thumb joints. E) Experimental paradigm of the pressing under 30% MVC force. F) Comparison of representative SNR results of the recruited subject for three different electrodes under maximum force. Data are plotted as means ± SD, $n = 3$. G) Time-frequency transform of the sEMG signals collected from the stretchable adhesive electrode. H) Time-frequency transform of the sEMG signals collected from the stretchable non-adhesive electrode. I) Time-frequency transform of the sEMG signals collected from the flexible non-stretchable electrode. Compared with the other two types of electrodes, the adhesive stretchable electrode can adhere to the skin surface with large deformation without the use of external tapes, and collect subtle sEMG signals with low motion artifacts.

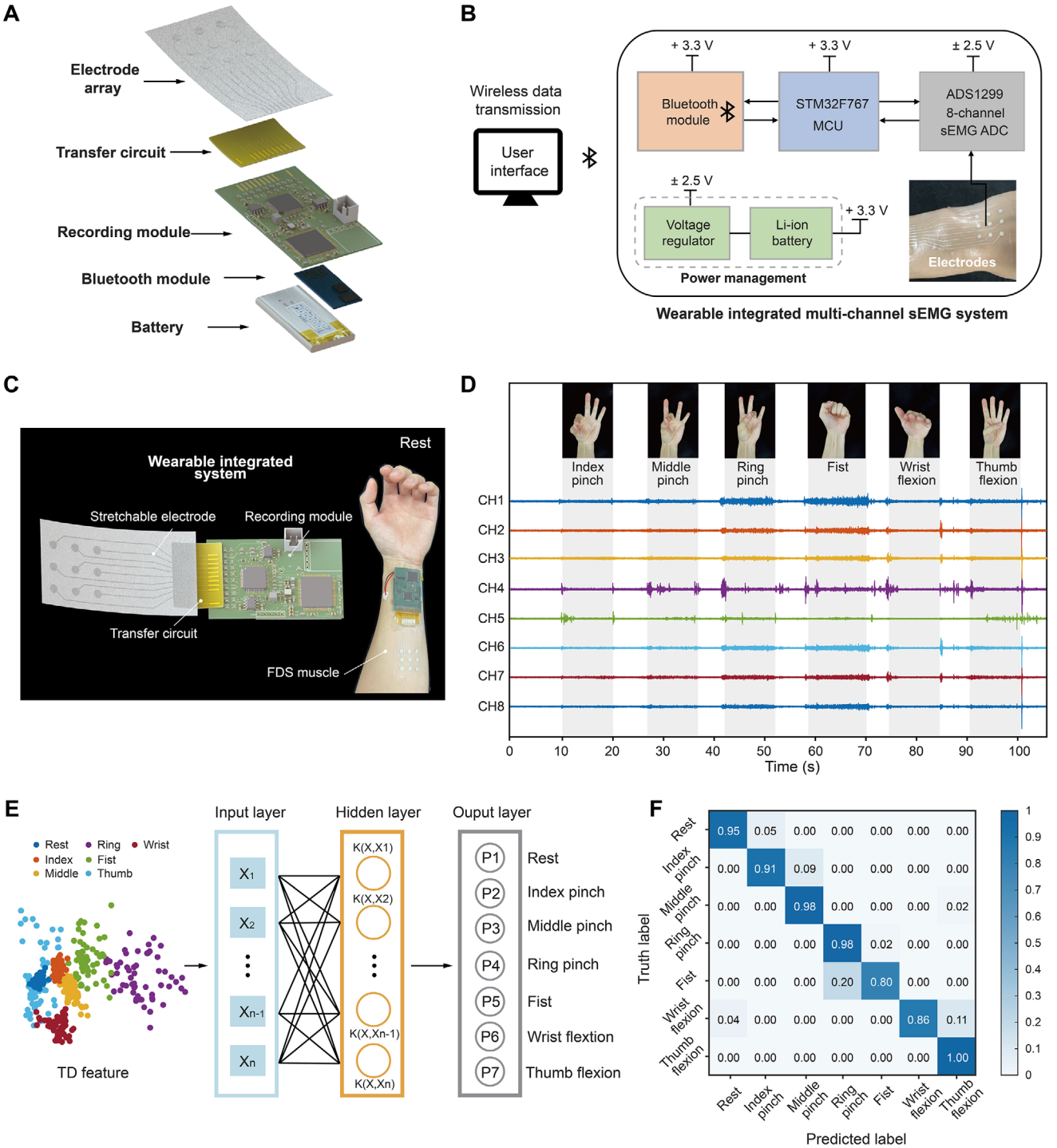

Figure 4. Design and application of the wearable integrated sEMG monitoring systems as the human-machine interface. A) The exploded view of the wearable, wireless integrated sEMG system. B) Block diagram of the wearable integrated sEMG system. C) Images showing the assembled wearable sEMG system and the experimental setup of hand gesture recognition with the wearable integrated system pasted on the forearm. D) Real-time monitoring of high-density sEMG signals of the forearm for various fine hand gestures. E) The framework of the machine learning method used for continuous hand gesture recognition based on the high-density sEMG signals. F) The confusion matrix of the continuous wrist-hand gesture recognition demonstrates an overall 92.6% classification accuracy.

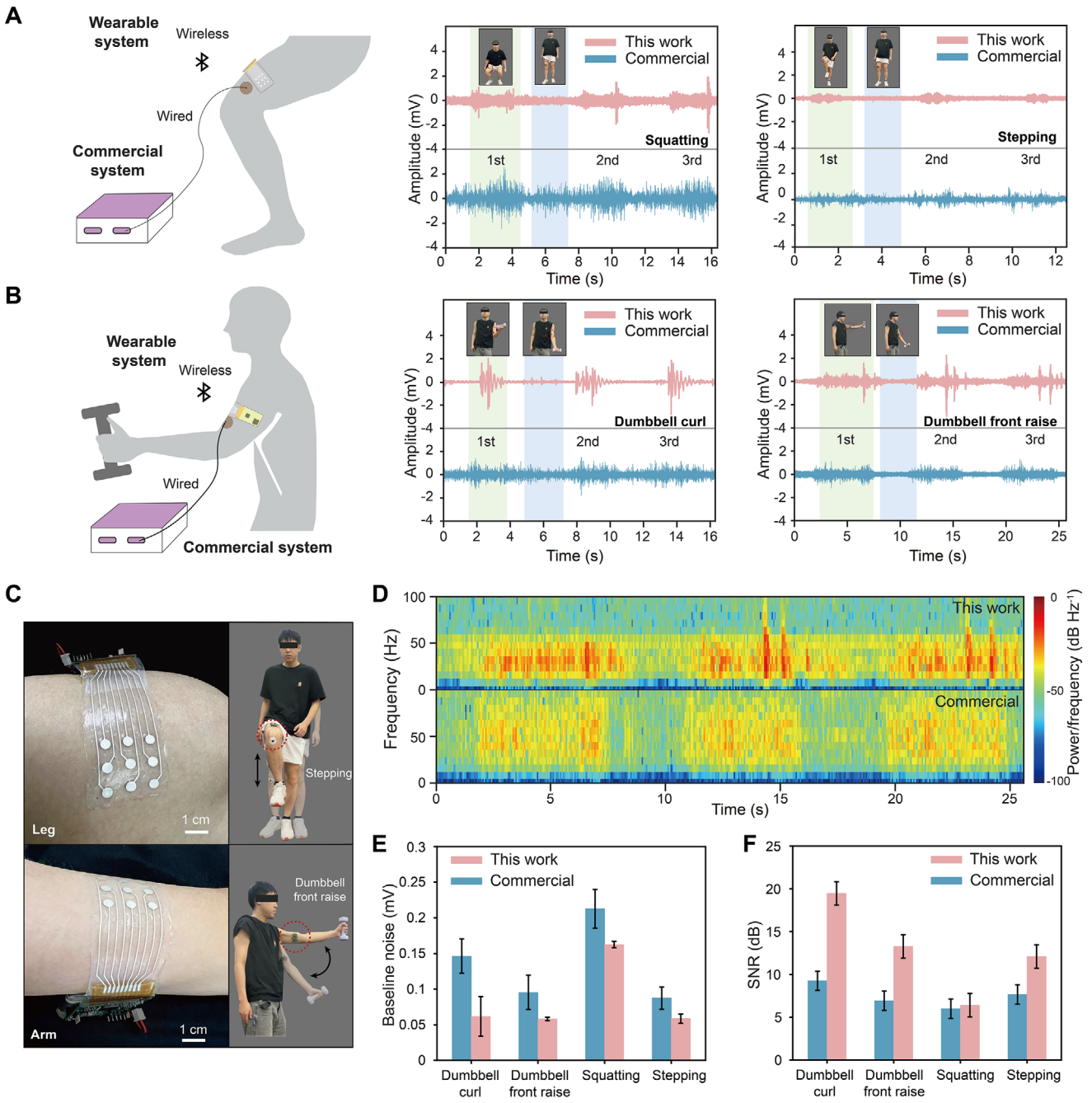

Figure 5. High-precision monitoring of high-density sEMG signals using wearable wireless sEMG system for dynamic exercises. A) The comparison of sEMG signals of the vastus medialis under dynamic tasks including squatting, and stepping. B) The comparison of sEMG signals of the biceps brachii under dynamic exercise including dumbbell curl, and dumbbell front raise. The commercial electrode system and wearable integrated electrode systems are applied to adjacent positions simultaneously. C) Images of two typical exercise training postures showing the superior conformal capability of the integrated system adhered to the leg and the upper arm respectively. D) Time-frequency transform of the sEMG signals of dumbbell front raises for two types of electrode systems. E) The comparison of the baseline noise between the wearable system and the commercial device. F) The comparison of the SNR between the wearable system and the commercial device.

Supporting Information). Figure 5C demonstrates the experimental scenarios of the wearable integrated sEMG human-machine interface adhered to the upper arm and leg for corresponding dynamic exercises. We further analyze the time-frequency sEMG signals of the dumbbell front raise (Figure 5D), demonstrating our wearable sEMG interface has stronger energy in the range of 0–100 Hz (the usable dominant frequency). Subtle signals of the rest state also reflect in the energy spectrum compared to the commercial one due to the weight of the dumbbell. Moreover, we calculate the baseline noise and the SNR of peak

sEMG signals. As shown in Figure 5E,F, our sEMG interface has clearer signals than the commercial system, which is attributed to less restriction on the human body and the resistance to motion artifacts. Thus, our wearable sEMG interface enables the collection of superior sEMG signals for dynamic exercise, showing the potential application for healthcare.

3. Conclusion

In this article, we report a wearable, wireless, and high-density sEMG interface consisting of 3D-printed multi-channel electrode arrays and a minimized wireless signal monitoring circuit. Our proposed three-layer sandwiched soft electrode arrays exhibit superior stretchability (≈150%) and adhesiveness (0.37 N cm^{-1}) based on continuous 3D printing. Owing to the reliable and conformal skin-electrode interface, our electrode presents the capability of motion artifact elimination and high SNR signal recording. We further integrate the high-density electrode array with a minimized wireless system to monitor multi-channel sEMG signals. Our integrated sEMG human-machine interface enables various wrist-hand gesture recognition through single muscle group detection and high-precision on-body monitoring under dynamic exercise.

4. Experimental Section

Materials: Ecoflex 0030, Ecoflex gel, and the release agent of silicone rubber (Ease release 200) were both purchased from Smooth-On. Stretchable Ag paste (JY12, 85% solid content, resistance 0.02 Ω sq^{-1} mil^{-1}) was purchased from Shanghai Julong Electronic Technology CO., LTD. The ink of Ecoflex 0030 was prepared by mixing parts A and B thoroughly for 3 min (1:1 by weight). The ink of Ecoflex gel was prepared by mixing parts A and B thoroughly for 2 min (1:3 by weight). The customized 3D printer had the negative pressure defoaming function to simplify the defoaming procedure of two types of inks. ACF tape (7303) was purchased from 3M. All the materials were used as received.

Optimization of the Adhesion Force: The mixing ratio of adhesive silicone ink was investigated to optimize interfacial adhesion strength. The results showed that the peeling force for the encapsulation layer increased as the decreasing proportion of the cross-linking agent (Figure S2, Supporting Information) while extending the curing time of Ecoflex gel. As a trade-off between adhesion and processing time, the cross-linking agent of 25 wt.% was chosen for the adhesive silicone. Figure S3 (Supporting Information) showed the adhesion ability of the optimal ratio of Ecoflex gel to various objects, such as the tangerine, wood cubes, and tapes.

Standard 90° Peeling Test: Five ratios of Ecoflex gel ink were prepared as 2:1, 1:1, 1:2, 1:3, and 1:4 respectively, where the former represented the cross-linking agent and the latter was the polymerizing agent. Then, the Ecoflex gel inks were molded into films with a thickness of 1 mm. To characterize the adhesion of different ratios of the Ecoflex gel, each film was adhered to a medical imitation skin to conduct a standard 90° peeling test based on the universal testing machine (INSTRON 6800) three times. The test was conducted at a peeling speed of 1 mm s^{-1}.

Integrated 3D Printing Process: The proposed integrated 3D printing process was depicted in Figure 2F. A square sacrificial PI layer was placed on the printing panel of our customized DIW 3D printer. Then, the release agent for silicone rubber called Ease release 200 was sprayed on the PI sacrificial layer to facilitate the detachment of electrode arrays after the end of fabrication. Later, the pretreated printing panel was placed on the printer, and the Ecoflex 0030 ink prepared on-site was filled into the printing syringe to print the base layer. Then, cured at room temperature for 10 min. Subsequently, the syringe filled with elastic Ag flakes ink was used to replace the Ecoflex 0030 syringe. Based on the predesigned patterns of electrode arrays, the conductive layer was printed continuously. To ensure the solvent of the stretchable silver wire was completely evaporated, 30 min were reserved for curing at 130 °C. Then, swapped the ink of the 3D printer to the on-site prepared Ecoflex gel ink, and printed the adhesive encapsulation layer. After 30 min of curing at 50 °C, the electrode array was plasma treated for 3 min to improve the adhesion of electrode connection pads to the ACF tape.

EIS Test: The recruited subjects consented to follow an approved protocol from the Institutional Review Board at Shanghai Jiao Tong University. They were required to place the forearm horizontally on the desk and wipe the skin with the alcohol. Four sizes of electrodes, diameter of 2, 3, 4, and 5 mm respectively, were printed for standard three-electrode impedance test. Each type of printed electrode was adhered to the same place of the skin with equal spacing, performing the EIS test by an electrochemical workstation (Autolab) three times.

Research on the Serpentine Design of the Printed Conductive Layer: The impact of the serpentine design on printing conductive wires was investigated. The serpentine line was defined by four main parameters:[44,45] diameter D, ribbon length L, curvature θ, and ribbon width W (Figure S21A, Supporting Information). To reduce research variables, the parameter of diameter D as 0.6 mm and ribbon width W as 0.15 mm was fixed. Modifying the curvature to change the structure of serpentine lines showed that the serpentine circuit changed from a horseshoe shape to a straight-line shape as the curvature decreased from 180° to 0° (Figure S20, Supporting Information). Then, conductive serpentine lines were printed, and the stretchability and resistance changes of serpentine lines with different structures were tested (Figure S21B, Supporting Information). The results showed that the printed serpentine conductive circuit would not significantly improve the stretchability of stretchable materials. Therefore, this study chose a straight line as the electrode connection line.

Integration of Wearable sEMG Monitoring Interface: The minimized recording module consisted of four parts including the EMG acquisition module, voltage module, MCU module, and ground module. The EMG acquisition module based on the biosignal monitoring chip of ADS1299 could achieve accurate monitoring of eight-channel signals at 1000 Hz by single-ended input mode. To avoid the static electricity of skin damaging the recording module, a protection circuit was also designed based on the OPA376 chip in the EMG acquisition module. The recorded EMG signals were transmitted to the MCU module through the SPI communication protocol in real-time. STM32F767 was chosen as the master chip due to the adequate memory space to avoid masking and loss of massive data. A Bluetooth module called HC-05 was used to achieve the transmission of packaged EMG data to the user interface. The voltage module was used to manage voltage requirements for functional modules, including 3.3, +2.5, and −2.5 V. The ground module was designed to connect digital ground, analog ground, and power ground to minimize signal inferences. The Bluetooth module was soldered to the recording module through the pin header. Double-sided foam tapes were responsible for bonding the Li-ion battery and recording circuit module. The electrode and adapter circuit were connected through ACF tape. The transfer circuit board and the acquisition circuit were connected by soldering. To achieve a stable connection between the skin and the wearable integrated system, the electrode was adhered to the skin through the adhesive encapsulation layer, and the recording circuit was bonded to the skin through double-sided adhesive foam tape.

Optical and SEM Observations: Optical images and videos of printed stretchable electrodes were captured by a GP-680 microscope (Gaopin). The morphologies of the printed stretchable Ag wires were characterized by a super-resolution field emission scanning electron microscope (FE-SEM) to achieve observation of the finest nanostructures.

sEMG Recording of the Commercial System: For the sEMG recording of the commercial system, two moist fabric straps were worn on the wrist to serve as the reference electrode and the ground electrode. A commercial disk electrode was connected to a multi-channel amplifier (Quattrocento, OT Bioelettronica) with a gain of 500 and a sampling frequency of 2048 Hz. The signals collected by the commercial amplifier were processed by the 10–500 Hz bandpass filter.

Statistical Analysis: All the mechanical properties presented in this study were measured from at least three parallel samples. Data distribution was assumed to be normal for all the parametric tests, but not formally tested, and no significant difference analysis was performed. The statistical analyses were carried out with the MATLAB R2020a software.

Supporting Information

Supporting Information is available from the Wiley Online Library or from the author.

Acknowledgements

This work was supported in part by the National Key R&D Program of China (Grant No. 2024YFB4707504), the National Natural Science Foundation of China (Grant No. 52025057), the Science and Technology Commission of Shanghai Municipality (Grant No. 24511103400) and Xplorer Prize.

Conflict of Interest

The authors declare no conflict of interest.

Data Availability Statement

The data that support the findings of this study are available from the corresponding author upon reasonable request.

Keywords

3D printing, human-machine interfaces, motion artifact, stretchable adhesive electrodes, wearable electronics

Received: March 31, 2025
Published online: May 4, 2025

[1] X. Navarro, T. B. Krueger, N. Lago, S. Micera, T. Stieglitz, P. Dario, *J. Peripher. Nerv. Syst.* **2005**, *10*, 229.
[2] G. Gu, N. Zhang, H. Xu, S. Lin, Y. Yu, G. Chai, L. Ge, H. Yang, Q. Shao, X. Sheng, X. Zhu, X. Zhao, *Nat. Biomed. Eng.* **2023**, *7*, 589.
[3] C. Xie, Q. Yang, Y. Huang, S. W. Su, T. Xu, R. Song, *IEEE Trans. Biomed. Circuits. Syst.* **2021**, *15*, 1332.
[4] G. Gu, N. Zhang, C. Chen, H. Xu, X. Zhu, *ACS. Nano.* **2023**, *17*, 9661.
[5] Y. Ma, Y. Zhang, S. Cai, Z. Han, X. Liu, F. Wang, Y. Cao, Z. Wang, H. Li, Y. Chen, X. Feng, *Adv. Mater.* **2020**, *32*, 1902062.
[6] L. Han, W. Liang, Q. Xie, J. Zhao, Y. Dong, X. Wang, L. Lin, *Adv. Sci.* **2023**, *10*, 2301180.
[7] X. Hu, A. Song, J. Wang, H. Zeng, W. Wei, *Sci. Data.* **2022**, *9*, 373.
[8] M. Cifrek, V. Medved, S. Tonković, S. Ostojić, *Clin. Biomech.* **2009**, *24*, 327.
[9] J. G. Webster, *IEEE Trans. Biomed. Eng.* **1984**, *31*, 823.
[10] J. Yin, S. Wang, T. Tat, J. Chen, *Nat. Rev. Bioeng.* **2024**, *2*, 541.
[11] N. Rodeheaver, R. Herbert, Y. S. Kim, M. Mahmood, H. Kim, J. W. Jeong, W. H. Yeo, *Adv. Funct. Mater.* **2021**, *31*, 2104070.
[12] Y. Liu, B. Xu, Z. Xie, J. Yang, Y. Liu, Y. Yang, H. Xu, *ACS Appl. Mater. Interfaces.* **2023**, *15*, 59787.
[13] D. Zhang, Z. Chen, L. Xiao, B. Zhu, R. Wu, C. Ou, Y. Ma, L. Xie, H. Jiang, *Microsyst. Nanoeng.* **2023**, *9*, 115.
[14] R. Garg, N. Driscoll, S. Shankar, T. Hullfish, E. Anselmino, F. Iberite, S. Averbeck, M. Rana, S. Micera, J. R. Baxter, F. Vitale, *Small. Methods.* **2023**, *7*, 2201318.
[15] Y. Jiang, Z. Zhang, Y. Wang, D. Li, C. Coen, E. Hwaun, G. Chen, H. Wu, D. Zhong, S. Niu, W. Wang, A. Saberi, J. Lai, Y. Wu, Y. Wang, A. A. Trotsyuk, K. Y. Loh, C. Shih, W. Xu, K. Liang, K. Zhang, Y. Bai, G. Gurusankar, W. Hu, W. Jia, Z. Cheng, R. H. Dauskardt, G. C. Gurtner, J. B. Tok, K Deisseroth, et al., *Science.* **2022**, *375*, 1411.
[16] M. Ramezani, J. H. Kim, X. Liu, C. Ren, A. Alothman, C. De-Eknamkul, M. N. Wilson, E. Cubukcu, V. Gilja, T. Komiyama, D. Kuzum, *Nat. Nanotechnol.* **2024**, *19*, 504.
[17] N. Driscoll, B. Erickson, B. B. Murphy, A. G. Richardson, G. Robbins, N. V. Apollo, G. Mentzelopoulos, T. Mathis, K. Hantanasirisakul, P. Bagga, S. E. Gullbrand, M. Sergison, R. Reddy, J. A. Wolf, H. I. Chen, T. H. Lucas, T. R. Dillingham, K. A. Davis, Y. Gogotsi, J. D. Medaglia, F. Vitale, *Sci. Transl. Med.* **2021**, *13*, abf8629.
[18] H. Lee, S. Lee, J. Kim, H. Jung, K. J. Yoon, S. Gandla, H. Park, S. Kim, *npj Flex. Electron.* **2023**, *7*, 20.
[19] Y. Li, N. Li, W. Liu, A. Prominski, S. Kang, Y. Dai, Y. Liu, H. Hu, S. Wai, S. Dai, Z. Cheng, Q. Su, P. Cheng, C. Wei, L. Jin, J. A. Hubbell, B. Tian, S. Wang, *Nat. Commun.* **2023**, *14*, 4488.
[20] H. Kim, J. Lee, U. Heo, D. K. Jayashankar, K. C. Agno, Y. Kim, C. Y. Kim, Y. Oh, S. H. Byun, B. Choi, H. Jeong, W. H. Yeo, Z. Li, S. Park, J. Xiao, J. Kim, J. W. Jeong, *Sci. Adv.* **2024**, *10*, 5260.
[21] Y. Yu, J. Li, S. A. Solomon, J. Min, J. Tu, W. Guo, C. Xu, Y. Song, W. Gao, *Sci. Robot.* **2022**, *7*, 0495.
[22] N. Kim, T. Lim, K. Song, S. Yang, J. Lee, *ACS Appl. Mater. Interfaces.* **2016**, *8*, 21070.
[23] J. Li, J. Cao, B. Lu, G. Gu, *Nat. Rev. Mater.* **2023**, *8*, 604.
[24] H. Yuk, X. Zhao, *Adv. Mater.* **2018**, *30*, 1704028.
[25] B. Lee, H. Cho, S. Moon, Y. Ko, Y. S. Ryu, H. Kim, J. Jeong, S. Chung, *Nat. Electron.* **2023**, *6*, 307.
[26] Y. Zhao, C. Chen, B. Lu, X. Zhu, G. Gu, *Adv. Funct. Mater.* **2024**, *34*, 2312480.
[27] A. Moin, A. Zhou, A. Rahimi, A. Menon, S. Benatti, G. Alexandrov, S. Tamakloe, J. Ting, N. Yamamoto, Y. Khan, F. Burghardt, L. Benini, A. C. Arias, J. M. Rabaey, *Nat. Electron.* **2021**, *4*, 54.
[28] Y. Song, R. Y. Tay, J. Li, C. Xu, J. Min, E. S. Sani, G. Kim, W. Heng, I. Kim, W. Gao, *Sci. Adv.* **2023**, *9*, 6492.
[29] S. Yang, J. Cheng, J. Shang, C. Hang, J. Qi, L. Zhong, Q. Rao, L. He, C. Liu, L. Ding, M. Zhang, S. Chakrabarty, X. Jiang, *Nat. Commun.* **2023**, *14*, 6494.
[30] H. Wang, Q. Ding, Y. Luo, Z. Wu, J. Yu, H. Chen, Y. Zhou, H. Zhang, K. Tao, X. Chen, J. Fu, J. Wu, *Adv. Mater.* **2024**, *36*, 2309868.
[31] R. Wan, J. Yu, Z. Quan, H. Ma, J. Li, F. Tian, W. Wang, Y. Sun, J. Liu, D. Gao, J. Xu, B. Lu, *Chem. Eng. J.* **2024**, *490*, 151454.
[32] G. Yang, K. Zhu, W. Guo, D. Wu, X. Quan, X. Huang, S. Liu, Y. Li, H. Fang, Y. Qiu, Q. Zheng, M. Zhu, J. Huang, Z. Zeng, Z. Yin, H. Wu, *Adv. Funct. Mater.* **2022**, *32*, 2200457.
[33] G. Yang, Z. Lan, H. Gong, J. Wen, B. Pang, Y. Qiu, Y. Zhang, W. Guo, T. Bu, B. Xie, H. Wu, *Adv. Funct. Mater.* **2025**, *35*, 2417841.
[34] G. Yang, Y. Hu, W. Guo, W. Lei, W. Liu, G. Guo, C. Geng, Y. Liu, H. Wu, *Adv. Mater.* **2024**, *36*, 2308831.
[35] H. Wu, G. Yang, K. Zhu, S. Liu, W. Guo, Z. Jiang, Z. Li, *Adv. Sci.* **2021**, *8*, 2001938.
[36] Y. Jiang, S. Ji, J. Sun, J. Huang, Y. Li, G. Zou, T. Salim, C. Wang, W. Li, H. Jin, J. Xu, S. Wang, T. Lei, X. Yan, W. Y. X. Peh, S. C. Yen, Z. Liu, M. Yu, H. Zhao, Z. Lu, G. Li, H. Gao, Z. Liu, Z. Bao, X. Chen, *Nature.* **2023**, *614*, 456.
[37] J. Cheng, J. Shang, S. Yang, J. Dou, X. Shi, X. Jiang, *Adv. Funct. Mater.* **2022**, *32*, 2200444.

[38] F. Ershad, M. Houston, S. Patel, L. Contreras, B. Koirala, Y. Lu, Z. Rao, Y. Liu, N. Dias, A. H. Garcia, W. Zhu, Y. Zhang, C. Yu, *PNAS. Nexus.* **2023**, *2*, 291.
[39] C. Li, T. Wang, S. Zhou, Y. Sun, Z. Xu, S. Xu, S. Shu, Y. Zhao, B. Jiang, S. Xie, Z. Sun, X. Xu, W. Li, B. Chen, W. Tang, *Research.* **2024**, *7*, 0366.
[40] M. R. Carneiro, C. Majidi, M. Tavakoli, *Adv. Funct. Mater.* **2022**, *32*, 2205956.
[41] H. Yuk, B. Lu, S. Lin, K. Qu, J. Xu, J. Luo, X. Zhao, *Nat. Commun.* **2020**, *11*, 1604.
[42] X. Peng, S. Wu, X. Sun, L. Yue, S. M. Montgomery, F. Demoly, K. Zhou, R. R. Zhao, H. J. Qi, *Adv. Mater.* **2022**, *34*, 2204890.
[43] E. Farago, D. MacIsaac, M. Suk, A. D. C. Chan, *IEEE Rev. Biomed. Eng.* **2022**, *16*, 472.
[44] Z. Yan, Y. Liu, J. Xiong, B. Wang, L. Dai, M. Gao, T. Pan, W. Yang, Y. Lin, *Adv. Mater.* **2023**, *35*, 2210238.
[45] Z. Huang, Y. Hao, Y. Li, H. Hu, C. Wang, A. Nomoto, T. Pan, Y. Gu, Y. Chen, T. Zhang, W. Li, Y. Lei, *Nat. Electron.* **2018**, *1*, 473.